

# Total scattering descriptions of local and cooperative distortions in the oxide spinel $\text{Mg}_{1-x}\text{Cu}_x\text{Cr}_2\text{O}_4$ with dilute Jahn-Teller ions

Daniel P. Shoemaker\* and Ram Seshadri†  
*Materials Department and Materials Research Laboratory,  
 University of California, Santa Barbara, CA, 93106, USA*

The normal spinel oxide  $\text{MgCr}_2\text{O}_4$  is cubic at room temperature while the normal spinel  $\text{CuCr}_2\text{O}_4$  is tetragonal as a consequence of the Jahn-Teller activity of  $\text{Cu}^{2+}$  on the tetrahedral sites. Despite different end-member structures, a complete solid solution of  $\text{Mg}_{1-x}\text{Cu}_x\text{Cr}_2\text{O}_4$  can be prepared with compounds of composition  $x = 0.43$  displaying a first-order phase transition at room temperature. Reverse Monte Carlo analysis of total neutron scattering on data acquired between 300 K and 15 K on samples with  $x = 0.10, 0.20$ , and  $0.43$  provides unbiased local and average structure descriptions of the samples, including an understanding of the transition from local Jahn-Teller distortions in the cubic phase to cooperative distortions that result in a tetragonal structure. Distributions of continuous symmetry measures help to understand and distinguish distorted and undistorted coordination around the tetrahedral site in the solid solutions. Magnetic exchange bias is observed in field-cooled hysteresis loops of samples with dilute  $\text{Cu}^{2+}$  concentration and in samples with tetragonal-cubic phase coexistence around 300 K.

PACS numbers: 71.70.Ej, 61.05.fm, 75.50.Tt

## INTRODUCTION

The propensity of octahedral  $\text{Cu}^{2+}$  ions in oxide structures to display Jahn-Teller (JT) distortions is intimately linked to magnetism and superconductivity in systems derived from  $\text{La}_2\text{CuO}_4$ . [1, 2] While less common, tetrahedral  $\text{Cu}^{2+}$  on the *A* site of oxide spinels can also display JT activity. This distortion lowers symmetry by compressing the tetrahedron and thereby breaking the degeneracy of the partially-occupied  $t_2$  energy levels. [3, 4] The crystal field splittings of the ideal and distorted tetrahedra are shown schematically in Fig. 1.

Jahn-Teller distortions themselves are an intriguing theme in functional materials because they enable interplay between electronic and structural degrees of freedom. They have been most widely studied in the manganites, often derivatives of perovskite  $\text{LaMnO}_3$ . [5–7] In these compounds,  $\text{Mn}^{3+}$  has four  $3d$  electrons with a singly-occupied pair of  $e_g$  states in an octahedral crystal field. It is well established that elongation of the octahedron breaks the degeneracy and lowers the energy of the system. [8, 9] The percolative nature of orbital ordering arising from cooperative JT distortion is believed to play a central role in colossal magnetoresistive behavior. [10]

In spinels, collective JT distortions on the *A* or *B* sites result in a reduction in symmetry from cubic  $Fd\bar{3}m$  to tetragonal  $I4_1/amd$  upon orbital ordering at the Jahn-Teller transition temperature  $T_{JT}$ . When only a fraction of occupied sites are JT-active, cation clustering can lead to endotaxial coexistence of tetragonal (distorted) and cubic phases, [11–13] with strain-driven checkerboard patterns first studied in phase-separated CoPt alloys. [14–16] These  $\text{Mn}^{3+}$ -driven JT distortions are a product of unpaired  $3d$  electrons, so self-assembled nanostructured magnetic films are under development. [17]

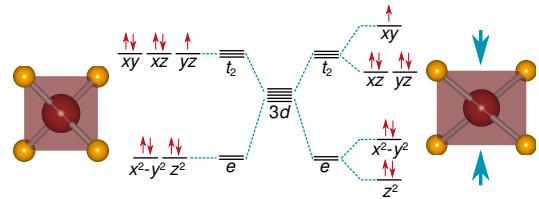


FIG. 1: (Color online) Crystal-field splitting of  $\text{Cu}^{2+}$  with a  $3d^9$  electron configuration in an ideal tetrahedron (left) results in degeneracy in the  $t_2$  orbitals. Jahn-Teller compression of the tetrahedron lifts the degeneracy (right), and results in a singly-occupied  $xy$  orbital.

Few studies have examined the precise JT tendency of  $\text{Cu}^{2+}$  on the spinel *A* site. The effect of  $\text{Cu}^{2+}$  occupancy on  $T_{JT}$  and the electronic or magnetic properties remains sparsely investigated. [18–20] We expect there should be key differences between JT activity on the *A* and *B* sites of spinel. While  $\text{BO}_6$  octahedra are edge-sharing and form a pyrochlore sublattice, the  $\text{AO}_4$  tetrahedra are isolated from each other in a diamond sublattice. The increased distance between *A* cations should hinder their cooperative behavior.

In this work, the structural effects of  $\text{Cu}^{2+}$  concentration  $x$  in the spinel solid solution  $\text{Mg}_{1-x}\text{Cu}_x\text{Cr}_2\text{O}_4$  are investigated by real- and reciprocal space structural probes utilizing total neutron scattering. Discrepancies between the average and local structural are of particular interest. Specifically, we probe whether the coordinations of JT-active  $\text{Cu}^{2+}$  and JT-inactive  $\text{Mg}^{2+}$  differ. Traditional Bragg diffraction analysis fails to resolve these differences because atoms on the same crystallographic site (here Cu and Mg on the spinel *A* site) are required to have identical surroundings. Electron paramagnetic resonance [21] and x-ray absorption [22] offer

a confirmation that dilute Jahn-Teller cations create local distortions, but these spectroscopic techniques do not yield any detailed structural information. We utilize the pair distribution function (PDF) because it provides a real-space description of the structure with distinct Cu–O and Mg–O distances.

Our previous PDF study of the spinel  $\text{CuMn}_2\text{O}_4$  encountered many of the complications that make  $\text{Mg}_{1-x}\text{Cu}_x\text{Cr}_2\text{O}_4$  a difficult crystal structure to describe. [23] In that study, Cu and Mn are present with mixed valence on both *A* and *B* positions, and the surrounding oxygen polyhedra are cation-dependent. We found that  $\text{CuO}_4$  tetrahedra are significantly more distorted (as judged by bond angles) than  $\text{MnO}_4$  tetrahedra, and Cu avoids the tendency for JT distortion by disproportionating to  $\text{Cu}^+/\text{Cu}^{3+}$ . The situation for  $\text{Mg}_{1-x}\text{Cu}_x\text{Cr}_2\text{O}_4$  should be less complex: no valence mixing is present, and Cu/Mg substitution is confined to the *A* site. The effect of central cation on  $\text{MO}_4$  distortion is more isolated.

We employ large box modeling via reverse Monte Carlo simulations as method of retrieving possible signatures of cation-dependent coordinations from the PDF. [24, 25] Supercells with thousands of atoms can be routinely simulated with modest computational requirements, and the large sample size provides element-specific information due to the presence of many discrete atoms of each type. A crucial aspect of RMC simulations is determining straightforward metrics that describe how local crystalline structure differs from the average. The tendency for distortion of individual polyhedra has been characterized by analyzing bond lengths, [23] bond angles, [23, 26, 27] and geometric analysis. [28, 29]

In this study, tetrahedral JT distortion is gauged using continuous symmetry measures (CSM). [30, 31] The particular strength of the CSM method is its ability to compare the symmetry of imperfect polyhedra, regardless of their size or orientation in space. [32, 33] Extraction of CSM information from RMC simulation was recently performed as a test of structural rigidity in  $\text{Bi}_2\text{Ti}_2\text{O}_7$  [34] and is employed here to compare the symmetry of  $\text{CuO}_4$ ,  $\text{MgO}_4$ , and  $\text{AA}_4$  tetrahedra, thereby describing the preference for JT activity as a function of *x* and temperature.

## METHODS

Powders of  $\text{Mg}_{1-x}\text{Cu}_x\text{Cr}_2\text{O}_4$  compounds were prepared by dissolving stoichiometric amounts of  $\text{Cu}(\text{NO}_3)_2 \cdot 2.5\text{H}_2\text{O}$ ,  $\text{Mg}(\text{NO}_3)_2 \cdot 6\text{H}_2\text{O}$ , and  $\text{Cr}(\text{NO}_3)_3 \cdot 9\text{H}_2\text{O}$  in water, followed by boiling to evaporate the solvent until a brown mass was formed, which was then ground and calcined in air at between 700°C or 1000°C for 10 hours, then cooled at 10°C/min. Laboratory X-ray diffraction patterns were acquired using Cu- $K_\alpha$  radiation on a Philips X’Pert diffractometer

at room temperature and a Bruker D8 diffractometer with an Anton Parr high-temperature stage. Magnetic properties were measured using a Quantum Design MPMS 5XL SQUID magnetometer. Time-of-flight (TOF) neutron scattering was performed on the NPDF instrument at Los Alamos National Laboratory. Rietveld refinements were performed using the XND code [35] for X-ray data and the GSAS-EXPGUI suite [36] for the TOF data. The PDF was extracted using the PDFGETN program [37] with  $Q_{\text{max}} = 35 \text{ \AA}^{-1}$  and least-squares refinement of the PDF was performed using the PDFGUI frontend for PDFFIT2. [38] Crystal structures were visualized with ATOMEYE [39] and VESTA. [40]

Reverse Monte Carlo simulations were run using RMCPROFILE version 6 [41] on  $7 \times 7 \times 7$  cubic or  $10 \times 10 \times 7$  tetragonal spinel supercells with 19208 or 19600 atoms, respectively. A hard-sphere repulsion was applied to prevent *M*–O bond distances shorter than the first peak of the PDF, but no clustering was observed at the cutoff distances. No preference for cation clustering was found, so configurations with randomized Cu and Mg occupancy were used. Simulations were performed as serial jobs on the HP Opteron QSR cluster at the California NanoSystems Institute.

Bond valence sums (BVS) were extracted from atoms in the supercell in the same manner described in our previous work on  $\text{CuMn}_2\text{O}_4$ , [23] using the  $R_0$  values of Brese and O’Keeffe. [42] CSM for  $\text{AO}_4$  tetrahedra were calculated using a distance measure program provided by M. Pinsky and D. Avnir.

## RESULTS AND DISCUSSION

### Average structure *via* reciprocal-space analysis

The compounds  $\text{MgCr}_2\text{O}_4$  and  $\text{CuCr}_2\text{O}_4$  both belong to the  $\text{AB}_2\text{O}_4$  spinel family of structures with the *A* cations,  $\text{Mg}^{2+}$  and  $\text{Cu}^{2+}$ , tetrahedrally coordinated by oxygen, while  $\text{Cr}^{3+}$  lies on the octahedral *B* site. The  $[\text{Ar}]3d^3$  electron configuration of  $\text{Cr}^{3+}$  is very stable because each of the  $t_{2g}$  energy levels is singly occupied, so there is no tendency of site mixing or mixed valence. [43] Varying *x* in  $\text{Mg}_{1-x}\text{Cu}_x\text{Cr}_2\text{O}_4$  therefore does not disturb the *B* sublattice composition, but changes in the interpenetrating *A* sublattice may lead to chemical pressure which will influence its size and shape.

On the tetrahedral *A* site,  $\text{Mg}^{2+}$  and  $\text{Cu}^{2+}$  have effectively identical ionic radii. Both are 0.57 Å as given by Shannon, [44] but their electron configurations are distinctly different.  $\text{Mg}^{2+}$  has the  $[\text{Ne}]$  configuration and no *d* electrons.  $\text{Cu}^{2+}$  has  $[\text{Ar}]3d^9$  and only two of the three  $t_2$  energy levels are fully occupied in tetrahedral coordination (Fig. 1). This degeneracy causes a JT distortion, manifested by a flattening of the tetrahedron. Bond lengths are preserved, but bond angles are no longer

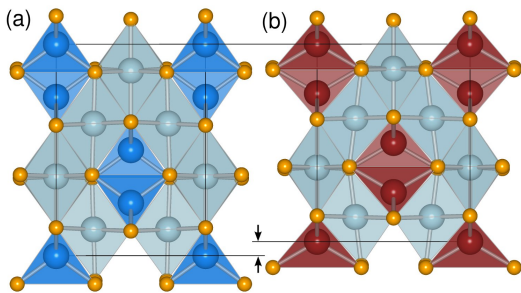


FIG. 2: (Color online) To scale, the pseudotetragonal cells of (a) cubic  $\text{MgCr}_2\text{O}_4$  and (b) Jahn-Teller distorted tetragonal  $\text{CuCr}_2\text{O}_4$  are viewed along the  $a$  axis of the  $I4_1/amd$  cell. Contraction in the  $c$  direction is evident due to JT distortion in  $\text{CuCr}_2\text{O}_4$ .  $\text{CrO}_6$  octahedra are light blue, while  $\text{MgO}_4$  and  $\text{CuO}_4$  tetrahedra are dark blue and red, respectively.

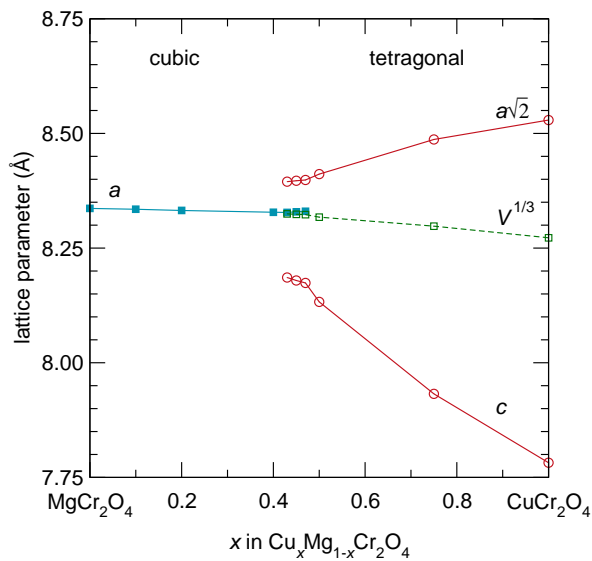


FIG. 3: (Color online) Lattice parameters of the  $\text{Mg}_{1-x}\text{Cu}_x\text{Cr}_2\text{O}_4$  solid solution obtained by Rietveld refinement of laboratory X-ray powder diffraction at room temperature. Coexistence of the cubic and tetragonal phases occurs for  $0.43 \leq x \leq 0.47$ .  $V^{1/3}$  is shown for tetragonal phases. Error bars are smaller than the symbols for all points.

equivalent at  $109.5^\circ$ . [45–47] The contrasting behavior of  $\text{Mg}^{2+}$  and  $\text{Cu}^{2+}$  in tetrahedral coordination is evident when the  $\text{MgCr}_2\text{O}_4$  and  $\text{CuCr}_2\text{O}_4$  structures are compared in Fig. 2.  $\text{MgCr}_2\text{O}_4$  forms in the cubic space group  $Fd\bar{3}m$  with ideal  $\text{MgO}_4$  tetrahedra. [48]  $\text{CuCr}_2\text{O}_4$  undergoes flattening in the  $c$  direction and forms in the tetrahedral space group  $I4_1/amd$ , which is the same space group as JT distorted  $\text{Mn}_3\text{O}_4$  (and other  $\text{AMn}_2\text{O}_4$ ) or  $\text{NiCr}_2\text{O}_4$ . [45, 49] The unit cells are shown to scale in Fig. 2 to highlight their difference in dimensions.

Alloying  $x$  from 0 to 1 in  $\text{Mg}_{1-x}\text{Cu}_x\text{Cr}_2\text{O}_4$  produces a transition from a cubic to tetragonal spinel. The lattice parameters obtained from Rietveld refinements to room-temperature XRD patterns shown in Fig. 3 reveal that

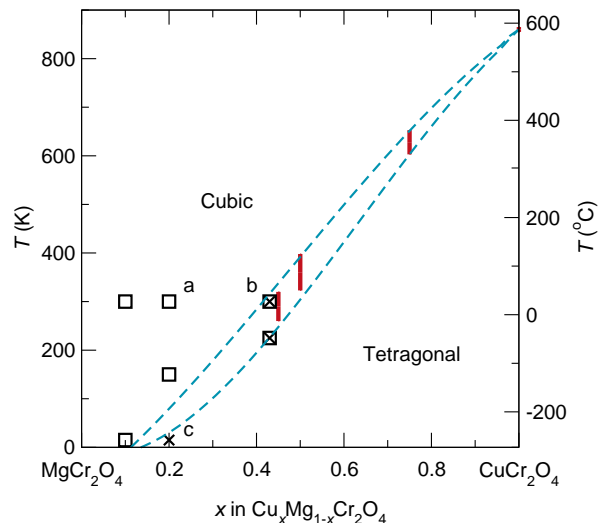


FIG. 4: (Color online) Phase diagram of the  $\text{Mg}_{1-x}\text{Cu}_x\text{Cr}_2\text{O}_4$  system as determined by Rietveld refinement. Points denote neutron refinements to cubic ( $\square$ ) and tetragonal ( $\times$ ) phases. Bars represent coexistence regions from high-temperature X-ray diffraction. Letters (a,b,c) correspond to the Rietveld refinements shown in Fig. 5.

for  $x < 0.43$  a cubic spinel is formed with a gradually decreasing lattice parameter  $a$ . When  $x = 0.43$  the tetragonal phase appears with  $c/a = 0.975$  and a small region of coexistence persists for  $0.43 \leq x \leq 0.47$ , above which the cubic phase disappears. The compound becomes increasingly tetragonal as the end member  $\text{CuCr}_2\text{O}_4$  is approached, with  $c/a = 0.912$  when  $x = 1$ . The pseudocubic cell volume contracts from  $579.4 \text{ \AA}^3$  for  $\text{MgCr}_2\text{O}_4$  to  $566.1 \text{ \AA}^3$  for  $\text{CuCr}_2\text{O}_4$ , which is a 2.3% decrease.

We extend our Rietveld analysis using high-temperature XRD and low-temperature TOF neutron scattering to produce an approximate phase diagram of the pseudobinary system  $\text{MgCr}_2\text{O}_4$ – $\text{CuCr}_2\text{O}_4$ , shown in Fig. 4. The  $T_{JT}$  between cubic and tetragonal spinels has a nearly linear relationship on  $x$ . There is some phase coexistence determined from HTXRD denoted by the bars on the graph. We use the end-member  $\text{CuCr}_2\text{O}_4$  transition of  $T_{JT} = 590^\circ\text{C}$  from the literature. [49, 50] The JT transition temperature steadily decreases with decreasing  $x$  so that the tetragonal phase occurs for  $x = 0.20$  but not for  $x = 0.10$  at  $T = 15 \text{ K}$  (the lowest temperature measured). Rietveld refinements to neutron scattering data are shown in Fig. 5 for three different points on the phase diagram, representing (a) cubic, (b) mixed, and (c) tetragonal phases at  $x = 0.20$  and  $T = 300 \text{ K}$ ,  $x = 0.43$  and  $T = 300 \text{ K}$ , and  $x = 0.20$  and  $T = 15 \text{ K}$ , respectively. In all cases, the fits are excellent. There is, however, some unfit intensity between split tetragonal peaks in (b) and (c), indicative of a more complex crystal structure than the two-phase Rietveld model would suggest.

Not shown on our phase diagram is the tetragonal dis-

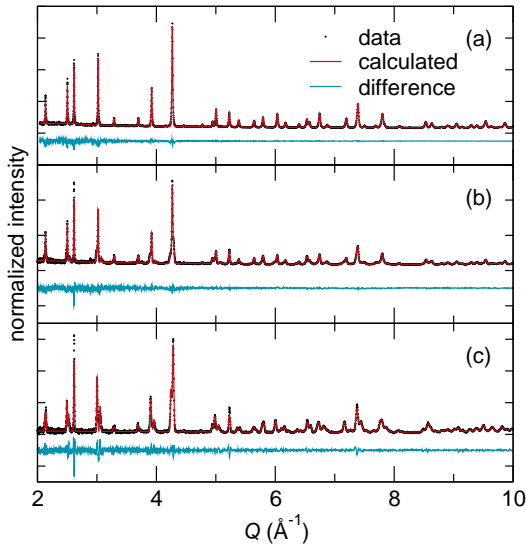


FIG. 5: (Color online) Time-of-flight neutron scattering Rietveld refinements of  $\text{Mg}_{1-x}\text{Cu}_x\text{Cr}_2\text{O}_4$  with (a)  $x = 0.20$  at 300 K [cubic], (b)  $x = 0.43$  at 300 K [cubic and tetragonal], and (c)  $x = 0.20$  at 15 K [tetragonal].

tortion around 12 K in  $\text{MgCr}_2\text{O}_4$ . [51–53] A transition from  $Fd\bar{3}m$  to  $I4_1/amd$  occurs to remove the geometric frustration of  $\text{Cr}^{3+}$  spins arranged in a pyrochlore sublattice. Addition of magnetic  $\text{Cu}^{2+}$  cations in the  $A$  sites should relieve this frustration due to strong  $A$ - $B$  interactions, [18, 54] so we do not expect the spin-driven distortion to play a role for  $x > 0$ . The sample with  $x = 0.10$  is cubic at 15 K.

The presence of a tetragonal phase for low  $\text{Cu}^{2+}$  content is surprising. At  $x = 0.20$ , for instance, only one in five  $A$  sites has a JT active cation. The  $A$  cations are arranged in a diamond sublattice and each has four nearest  $A$  neighbors. The tetrahedra do not share edges or corners with each other, with the shortest exchange pathway being  $A\text{--O--Cr--O--A}$ . Given a random cation distribution, the probability of one  $\text{Cu}^{2+}$  having all JT-inactive  $\text{Mg}^{2+}$  neighbors is  $(\frac{4}{5})^4 = 41.0\%$ . The probability of having only one  $\text{Cu}^{2+}$  neighbor is  $4(\frac{1}{5})(\frac{4}{5})^3 = 41.0\%$ , and the probability of having two  $\text{Cu}^{2+}$  neighbors falls to  $6(\frac{1}{5})^2(\frac{4}{5})^2 = 15.4\%$ . Thus 82.0% of  $\text{Cu}^{2+}$  cations have zero or only one JT-active nearest neighbor, but they still produce orbital ordering with long-range periodicity. The trend of  $T_{JT}$  versus  $x$  is roughly linear in Fig. 4, with no apparent jump at the percolation threshold of the diamond-type  $A$  sublattice. [55, 56]

The critical concentration of  $\text{Cu}^{2+}$  needed to drive a cooperative JT distortion in  $\text{Mg}_{1-x}\text{Cu}_x\text{Cr}_2\text{O}_4$  at 300 K is  $x = 0.43$ . This fraction increases with  $A$ -site cation radius in  $\text{ACr}_2\text{O}_4$  spinels:  $\text{Zn}_{1-x}\text{Cu}_x\text{Cr}_2\text{O}_4$  ( $r_{\text{Zn}} = 0.60$  Å) is reported to have  $x = 0.47$  [57] and  $x = 0.58$ , [18] while  $\text{Cd}_{1-x}\text{Cu}_x\text{Cr}_2\text{O}_4$  ( $r_{\text{Cd}} = 0.78$  Å) has  $x = 0.64$ . [20] This could be due to increased distance between  $A$ -site

cations, or a loosening of the structure (thus weakening of strain field produced by a JT distortion).

The critical concentration in  $\text{Zn}_{1-x}\text{Ni}_x\text{Cr}_2\text{O}_4$ , [58] where  $\text{Ni}^{2+}$  drives JT distortion, is around  $x \sim 1$  at room temperature. For  $\text{Cr}^{3+}$  on the spinel  $B$  site, less  $\text{Cu}^{2+}$  is needed to drive a cooperative distortion than  $\text{Ni}^{2+}$ . The  $3d^8$  configuration of  $\text{Ni}^{2+}$  has only one unpaired  $t_2$  electron, rather than the two of  $\text{Cu}^{2+}$ . The result is a smaller energy gain after breaking degeneracy and elongation (rather than contraction) of the  $c$  axis. [4]

Comparison with JT tendency of  $\text{Mn}^{3+}$  on the spinel  $B$  site is less direct. For example, the solid solution  $\text{Zn}[\text{Fe}_{1-x}\text{Mn}_x]_2\text{O}_4$  has a critical concentration of about  $x = 0.3$ , [59] while  $\text{Mn}[\text{Cr}_{1-x}\text{Mn}_x]_2\text{O}_4$  has  $x = 0.4$ . [60] This would seem to indicate a stronger JT tendency, in part due to closer  $B$ - $B$  distances and edge sharing between octahedra. However, for  $\text{Zn}_{x/2}\text{Ge}_{1-x/2}[\text{Co}_{1-x}\text{Mn}_x]_2\text{O}_4$ , Wickham reports  $x = 0.65$ , [61] and Bhandage reports  $x = 0.70$  for  $\text{Zn}_{x/2}\text{Mn}_{1-x/2}[\text{Ni}_{1-x}\text{Mn}_x]_2\text{O}_4$ . [62] The wide spread in critical concentrations of  $\text{Mn}^{3+}$  can be explained by the differences in JT splitting energies found by X-ray absorption spectroscopy on  $\text{AMn}_2\text{O}_4$  spinels by Noh, *et al.* [22] In essence, the energy drop from JT distortion around  $\text{Mn}^{3+}$  on the spinel  $B$  site is very sensitive to changes in chemical pressure.

We obtain the *cooperative* behavior of the averaged lattice using Rietveld refinement. We do not necessarily resolve the distinct cation coordinations of  $\text{Mg}^{2+}$  and  $\text{Cu}^{2+}$  if they are different on the local, atomic length scale. Two views of the JT transition can be proposed: in the case of a sharp crossover, as would be implied by how Rietveld analysis is performed, all  $\text{AO}_4$  tetrahedra are equivalent whether they contain  $\text{Mg}^{2+}$  or  $\text{Cu}^{2+}$ , and upon increasing  $x$  they abruptly transform from ideal tetrahedra in the cubic spinel to flattened tetrahedra in the cooperatively JT distorted spinel. In the second case, the  $\text{CuO}_4$  tetrahedra are *always* locally JT distorted (even for values of  $x$  where the spinel is cubic) but the crossover at  $x = 0.43$  at room temperature represents the point where they cooperatively order and the JT distortions percolate through the long-range structure.

### Local structure *via* real-space analysis

The average structure model of  $\text{Mg}_{1-x}\text{Cu}_x\text{Cr}_2\text{O}_4$  from Rietveld refinement indicates that the compounds exist as single phases, either cubic or tetragonal, apart from the two-phase coexistence region around  $T_{JT}$ . When modeled using a single unit cell,  $\text{Mg}^{2+}$  and  $\text{Cu}^{2+}$  are required to share the same crystallographic site and their surroundings are necessarily identical. This model often inadequately describes the true structure of compounds where energy-lowering changes in cation coordination are known to persist above the average structural transition temperature as in perovskite manganites and cobaltites.

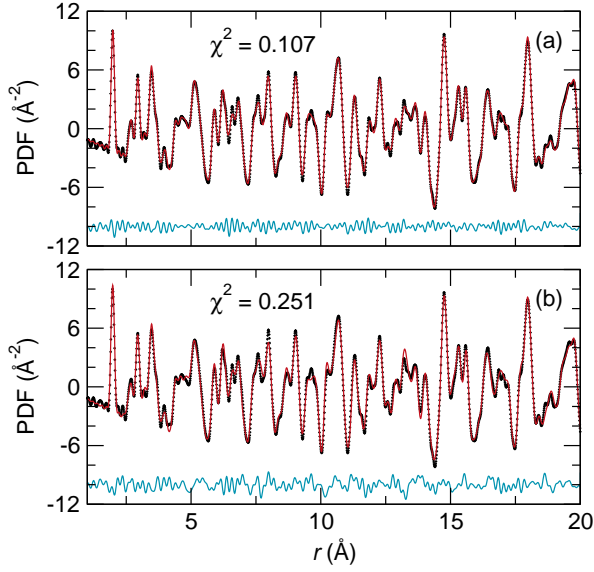


FIG. 6: (Color online) Least-squares fits to the PDF for  $x = 0.20$  at 300 K for the (a) cubic spinel phase with fractional-occupancy obtained from Rietveld refinement, and (b) an 80-20 fit to the end members  $\text{MgCr}_2\text{O}_4$  and  $\text{CuCr}_2\text{O}_4$ .

[5, 6, 63, 64] The PDF has emerged as a key tool for measuring these local distortions that do not possess long-range order. Because the PDF is a weighted histogram of all atom-atom distances in the sample, it is sensitive to the distinct bond distances that are produced by dissimilar coordination of multiple chemical species on the same site.[23] We investigate whether the PDF shows any signature of distinct  $\text{Cu}^{2+}$  and  $\text{Mg}^{2+}$  coordination.

Least-squares PDF refinements can be performed using the average structure unit cells from Rietveld refinement as a starting point. Fits to the  $x = 0.20$  data at 300 K are shown in Fig. 6. Panel (a) shows the fit to a Rietveld-refined cubic unit cell with split 0.20/0.80 occupancy of  $\text{Cu}^{2+}$  and  $\text{Mg}^{2+}$  on the same crystallographic site. In (b), we fit using a 0.20/0.80 linear combination of the  $\text{MgCr}_2\text{O}_4$  and  $\text{CuCr}_2\text{O}_4$  end members with lattice parameters allowed to refine. The fit is good despite the use of a tetragonal unit cell to model a structure far above  $T_{JT}$ , but it does not improve on the fit using a single cubic unit cell. We use the value

$$\chi^2 = \sum \frac{(\text{PDF}^{\text{obs}} - \text{PDF}^{\text{calc}})^2}{N} \quad (1)$$

to compare fits, where  $N$  is the number of points in the PDF from the nearest-neighbor cutoff to 20 Å. The ability to distinguish Mg and Cu is hindered by their similar neutron scattering lengths: 5.38 and 7.71 fm, respectively.[65] For  $x = 0.20$ , least-squares PDF fits do not definitively prove that there are distinct (or identical) coordination environments for  $\text{Mg}^{2+}$  and  $\text{Cu}^{2+}$ .

Resolution of distinct cation environments is aided when  $x = 0.43$  due to approximately even concentra-

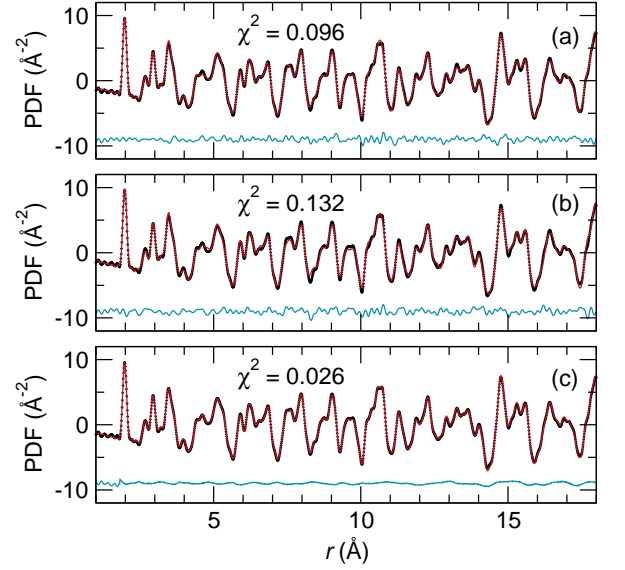


FIG. 7: (Color online) Fits to the PDF for  $x = 0.43$  at 300 K for (a) least-squares refinement of the two fractional-occupancy phases found from Rietveld refinement, (b) least-squares refinement using the end members  $\text{MgCr}_2\text{O}_4$  and  $\text{CuCr}_2\text{O}_4$ , and (c) the fit after RMC simulation.

tions of  $\text{Cu}^{2+}$  and  $\text{Mg}^{2+}$ . At 300 K, Rietveld refinement found coexistence of the cubic and tetragonal phases. Neither phase alone can be used to produce a satisfactory fit to the PDF. A two-phase fit using the Rietveld refined cells is shown in Fig. 7(a), and agrees quite well with the data. As with the  $x = 0.20$  sample, we also fit the data to a combination of the end members  $\text{MgCr}_2\text{O}_4$  and  $\text{CuCr}_2\text{O}_4$  in Fig. 7(b). Again, the fractional occupancy Rietveld result produces a better fit than the end members. The least-squares fits indicate that the average structures produce excellent representations of the local structures, but they do not definitively show whether the  $\text{Mg}^{2+}$  and  $\text{Cu}^{2+}$  coordination environments are distinct or similar.

Least-squares fits to the PDF are required to specify how many distinct  $\text{AO}_4$  environments to allow, much like in a Rietveld refinement. The  $Fd\bar{3}m$  and  $I4_1/amd$  unit cells provide only one  $\text{AO}_4$  environment per phase. There is no way to define cation-dependent coordination without manually building a lower-symmetry unit cell. In order to investigate the  $\text{AO}_4$  environment directly, we remove the symmetry constraints of least-squares PDF analysis and utilize large-box modeling via reverse Monte Carlo (RMC) simulations. This method has proved to be useful for investigating atomic structure on the local level, especially in cases where long-range periodicity is not present, such as  $\text{SrSnO}_3$ ,[28]  $\text{Bi}_2\text{Ti}_2\text{O}_7$ ,[34] and  $\beta$ -cristobalite.[66]

The RMC supercell for an  $x = 0.20$  sample at 15 K is inspected by folding each of the unit cells back into a single box, shown in Fig. 8, which reveals how each crys-



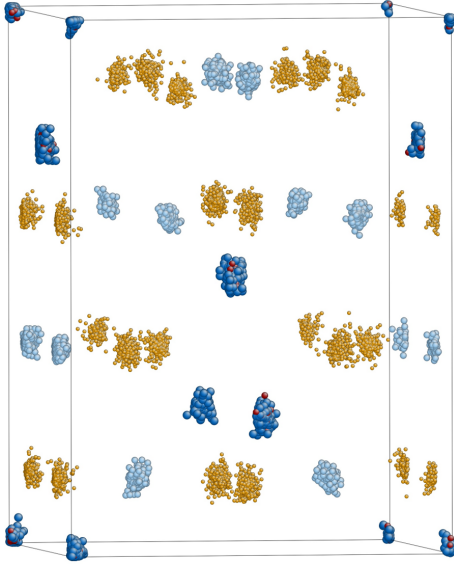


FIG. 8: (Color online) The final  $10 \times 10 \times 7$  RMC supercell for an  $x = 0.20$  simulation is folded into a single unit cell to obtain point clouds at each crystallographic site. Atoms shown are Cu (red), Mg (dark blue), Cr (light blue), and O (orange).

tallographic site is decorated with atoms. The supercell contains 560 Cu and 2240 Mg atoms that are randomly arranged. Because there are a large number of distinct Cu and Mg atoms, statistical analysis can be used to investigate whether there is any evidence for the local  $AO_4$  distortion to depend on the central cation. Bond valence sum histograms shown in Fig. 9 show that both the  $A$  cations have valences peaked around the expected value of  $A^{2+}$ , and the  $B$  site shows only  $Cr^{3+}$ , which implies that our supercells contain chemically reasonable bond lengths.

No cation dependence of  $AO_4$  bond distances is obvious from partial radial distributions  $g_{Cu-O}(r)$  and  $g_{Mg-O}(r)$ . This is to be expected because  $Mg^{2+}$  and  $Cu^{2+}$  have the same ionic radius when tetrahedrally coordinated. Neither is there any apparent distinction between  $CuO_4$  and  $MgO_4$  tetrahedra based upon O-A-O bond angles, in contrast to our previous study on  $CuMn_2O_4$ . [23]

We use the continuous symmetry measure (CSM) technique to gauge the tendency for JT distortion of  $AO_4$  tetrahedra. The CSM technique provides a distance measure (DM) of a given tetrahedron that indicates its deviation from ideality. [30, 31] A perfect tetrahedron has  $DM = 0$ , and any distortion increases the value of DM. In the end member compounds,  $MgO_4$  has a  $DM = 0$  while  $CuO_4$  has a  $DM = 0.0076$ . Having thousands of distinct tetrahedra in the RMC supercell affords the opportunity to produce a histogram of DM (Fig. 10) for all tetrahedra depending on the central cation. Each panel contains eight lines: four for each cation, resulting from four in-

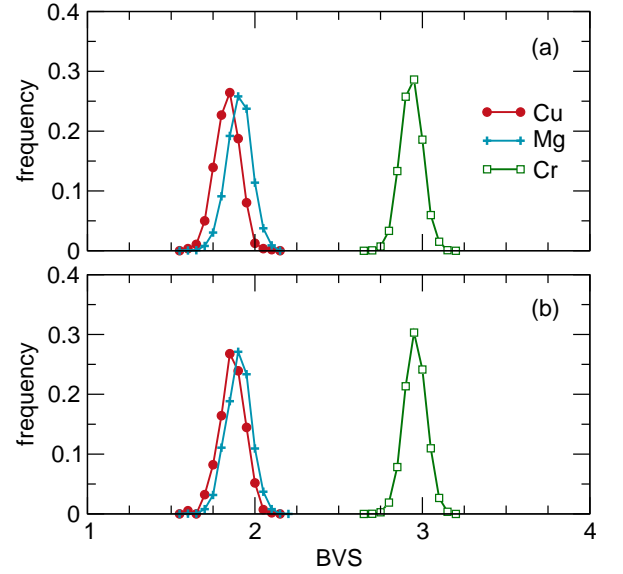


FIG. 9: (Color online) Bond valence sums for Cu and Mg extracted from  $Mg_{1-x}Cu_xCr_2O_4$  RMC supercells  $x = 0.20$  after fits to data at  $T = 300$  K (a) and  $15$  K (b). Aside from a slight broadening at  $300$  K, the distributions are comparable.

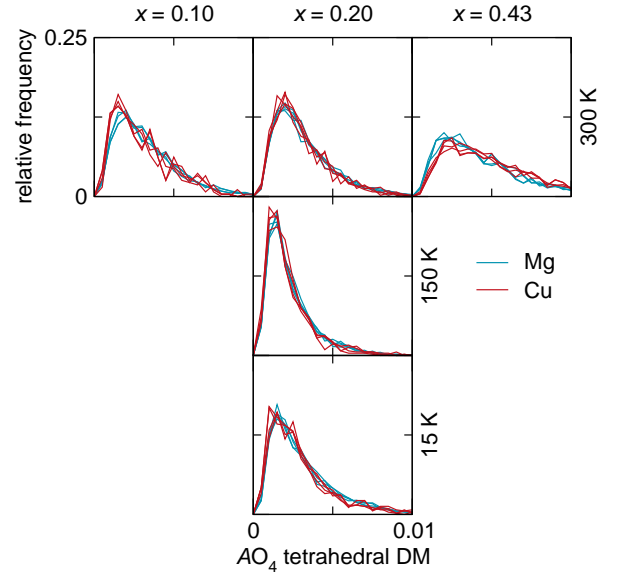


FIG. 10: (Color online) CSM histograms from RMC simulations for three Cu contents and three temperatures. Each panel contains 8 distributions: one Cu and one Mg for four independent simulations. Broadening across the  $T = 300$  K series indicates increasing tetrahedral distortion with  $x$ . Thermal effects lead to sharpening and shifting toward smaller DM when the  $x = 0.20$  sample is cooled to  $150$  K. This tendency toward ideal tetrahedra is disrupted by long-range tetragonal distortion upon further cooling, so the  $T = 15$  K histogram is broad and shifted to higher DM.

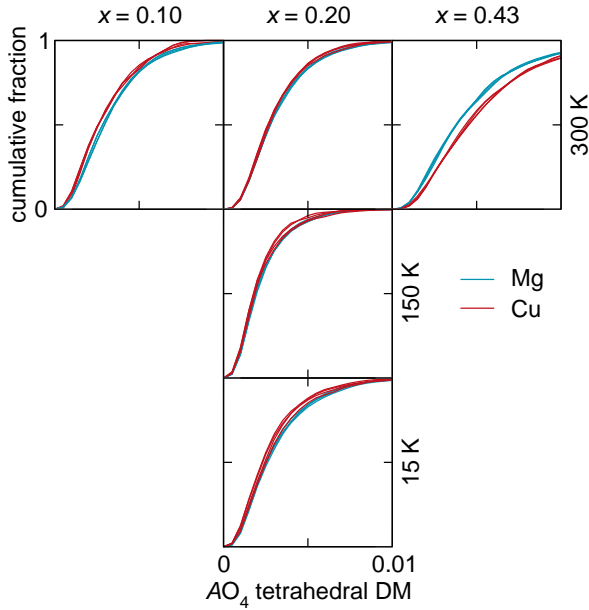


FIG. 11: (Color online) Cumulative CSM distributions are similar enough from run to run that most lines overlay each other. Only the  $x = 0.43$  run has a clear distinction between  $\text{CuO}_4$  and  $\text{MgO}_4$  tetrahedron shape, with  $\text{MgO}_4$  distinctly more ideal than  $\text{CuO}_4$ .

dependent RMC simulations. The overall shape of each histogram describes the average distortion (peak center) and the tightness of the DM distribution (peak width) at each value of  $x$  and  $T$ . No tetrahedra are present with exactly  $\text{DM} = 0$  because stochastic RMC simulations leave no atomic positions untouched—even a compound with ideal tetrahedra would have the shapes subtly distorted.

At 300 K, the spread of distortions increases for  $x = 0.43$  because the average structure becomes a mixture of cubic and tetragonal phases. In the series where  $x = 0.20$ , the peak sharpens upon cooling to 150 K, which we attribute to a reduction of thermal vibrations. It also moves to smaller DM values, indicating a tendency toward a more ideal  $\text{MO}_4$  environment. This trend would continue to low temperature in the absence of long-range JT distortion. Instead, the peak broadens and shifts to higher DM at 15 K. We attribute both of these effects to the tetragonal phase transition. These histograms provide a view of the average tetrahedral shape, but no distinction between Mg and Cu is apparent. We find that cumulative distributions offer a clearer picture of this dependence.

The cumulative distributions in Fig. 11 do not show separation between the Cu and Mg curves in the  $x = 0.10$  or  $0.20$  samples. However, the  $x = 0.43$  sample shows a clear distinction, with Mg tetrahedra possessing DM that are closer to zero (more ideal) than Cu. This is clear evidence for the tendency of Cu to undergo JT distortion while Mg remains more symmetric.

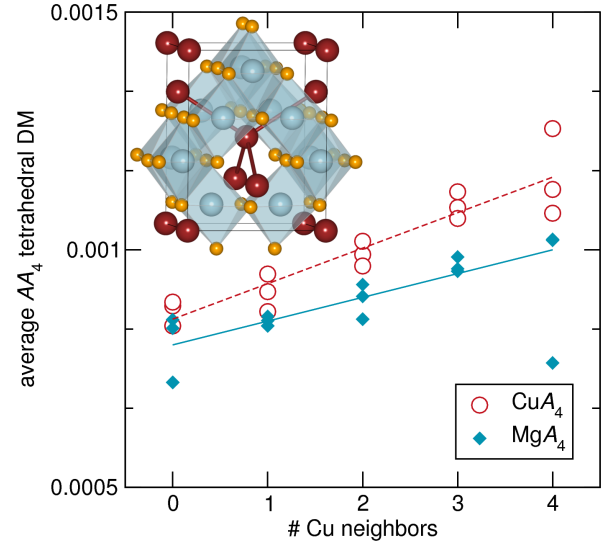


FIG. 12: (Color online) CSM distributions of  $\text{AA}_4$  tetrahedra (connected by long red bonds in inset) as a function of number of neighbors that are JT-active  $\text{Cu}^{2+}$ . Distinct distributions are shown for  $\text{CuA}_4$  (circles) and  $\text{MgA}_4$  (diamonds). Linear guides to the eye for each distribution show increasing tetrahedral distortion with number of Cu neighbors, and overall more distorted tetrahedra when tetrahedra are Cu-centered.

Overlapping DM curves for  $x = 0.10$  and  $0.20$  do not preclude the possibility of distinct  $\text{CuO}_4$  and  $\text{MgO}_4$  tetrahedra in those samples. There may be insufficient resolution in the PDF to distinguish the cations due to their similar neutron scattering cross sections and the relatively low concentration of  $\text{Cu}^{2+}$ . It remains unclear whether distinct cation environments are only seen around  $x = 0.5$  (due to approximately even cation concentrations) and if the distinction would disappear as  $x \rightarrow 1$ . Temperature dependence of the CSM when  $x = 0.43$  may also provide some insight into the dynamics of these distortions. Substituting a JT-inactive  $A$  site cation with a different neutron scattering cross length, such as  $\text{Mn}^{2+}$  or  $\text{Co}^{2+}$ , may aid contrast with  $\text{Cu}^{2+}$ .

Short-range interactions between JT-active cations are evident in the  $A$ - $A$  correlations in Fig. 12. Each  $A$  cation has four  $A$  nearest neighbors  $3.59 \text{ \AA}$  away, arranged in a diamond lattice (inset in Fig. 12). The four nearest neighbors create a large tetrahedron around the central cation. The tetrahedral DM for these  $\text{AA}_4$  are plotted for each central cation (Mg or Cu) as a function of the number of Cu nearest neighbors, from 0 to 4. Multiple RMC simulations show an upward trend indicating more distortion as the number of nearby Cu increases. The separation between the two lines implies that Cu-centered  $\text{CuA}_4$  have higher tetrahedral DM (more distortion) than Mg-centered  $\text{MgA}_4$ . These short-range correlations are indicative of strain coupling between adjacent  $A$ -site JT distortions.

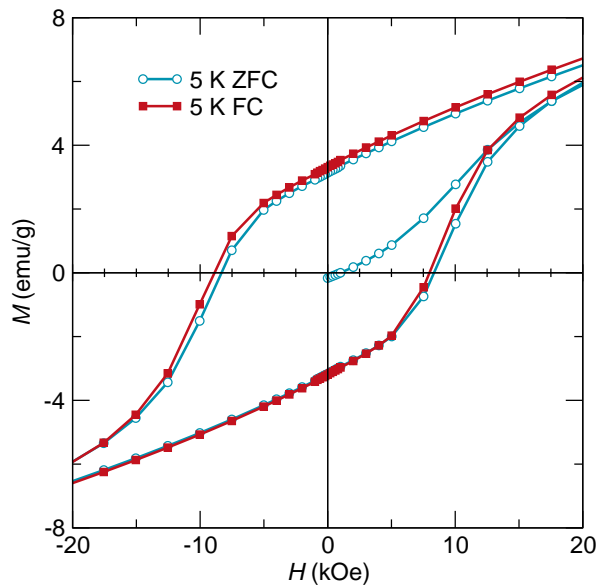


FIG. 13: (Color online) Magnetic hysteresis of  $\text{Mg}_{1-x}\text{Cu}_x\text{Cr}_2\text{O}_4$  with  $x = 0.43$  at  $T = 5$  K after zero-field cooling (ZFC) and field cooling (FC) with  $H_{FC} = 5$  T. The shift in the  $-H$  direction when  $M = 0$  is the exchange bias field  $H_E$ .

### Magnetic properties

$\text{MgCr}_2\text{O}_4$  and  $\text{CuCr}_2\text{O}_4$  have markedly different magnetic behavior due to the addition of unpaired spins in  $\text{Cu}^{2+}$  and the accompanying JT distortion.  $\text{CuCr}_2\text{O}_4$  is a hard ferrimagnet with  $T_C = 135$  K,[67] while  $\text{MgCr}_2\text{O}_4$  undergoes complex antiferromagnetic ordering below  $T_N = 16$  K.[53, 68] Macroscopic composites of a ferromagnet and antiferromagnet would result in a traditional exchange biased material, with an enhanced coercive field  $H_C$  and an exchange bias field  $H_E$ , manifested as a shift of the hysteresis loop in the  $-H$  direction.[69–71]

The  $\text{Mg}_{1-x}\text{Cu}_x\text{Cr}_2\text{O}_4$  solid solution is a mixture on the atomic level, but nevertheless exhibits the magnetic hallmarks of an exchange biased system. The hysteresis loop of the  $x = 0.43$  sample in Fig. 13 at  $T = 5$  K has  $H_C = 8.4$  kOe. Cooling with a field  $H_{FC} = 50$  kOe broadens the hysteresis loop and shifts it in the  $-H$  direction by  $H_E = 0.44$  kOe. This shift signifies the preference for the ferrimagnet to align along the field-cooling direction.  $H_C$  and  $H_E$  decrease with the  $\text{Cu}^{2+}$  concentration  $x$ , as does the onset of magnetic ordering. These trends are shown in Fig. 14. In all cases, field-cooling increases  $H_C$  and results in the appearance of a significant  $H_E$ . We find  $H_E = 0$  in all samples after zero-field cooling.

Exchange bias is traditionally manifested by pinning at the interface between a ferro- or ferrimagnet and antiferromagnet after field cooling when  $T_C > T_N$ . It can also arise from intrinsic disorder in a single-phase system, or the presence of disordered spins from either a spin glass

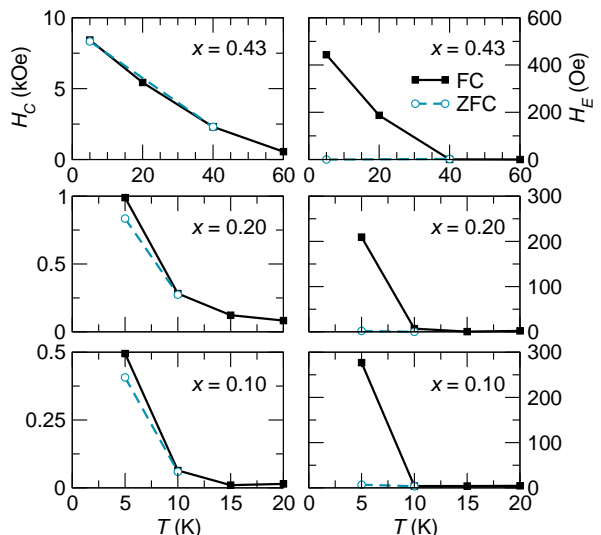


FIG. 14: (Color online) Coercive fields  $H_C$  (left) and exchange bias fields  $H_E$  (right) for  $\text{Mg}_{1-x}\text{Cu}_x\text{Cr}_2\text{O}_4$  samples with  $x = 0.43, 0.20$ , and  $0.10$  after ZFC and FC with  $H_{FC} = 5$  T. In all cases, ZFC results in a smaller  $H_C$  and gives  $H_E = 0$ .

or uncompensated surface spins on small particles (which behave in a glassy manner themselves).[72, 73] In the  $\text{Mg}_{1-x}\text{Cu}_x\text{Cr}_2\text{O}_4$  system, the magnetic behavior cannot be fully described by traditional AFM-FM interplay between  $\text{MgCr}_2\text{O}_4$  and  $\text{CuCr}_2\text{O}_4$  because the onset of  $H_E$  when  $x = 0.43$  in Fig. 14 occurs above  $T = 20$  K, which is above the Néel temperature of  $\text{MgCr}_2\text{O}_4$ . Therefore the disordered solid solution contains some regions of heterogeneity which may behave as glassy moments or as some intermediate AFM phase. Either of these cases can produce exchange bias. [18, 74]

The correlations between  $A$  cations seen in Fig. 12 indicate that the local structure varies with the composition of nearby atoms. Magnetic interactions, in turn, will be affected by these local distortions. A more detailed investigation of magnetic behavior, as was performed on  $\text{Zn}_x\text{Mn}_{3-x}\text{O}_4$ , [55] may help elucidate how the competing structural and magnetic interactions produce exchange bias. The phenomenon of JT-active cation clustering has been investigated by dilatometry, [75] but its effects on magnetism have not been explored in detail.

### CONCLUSIONS

We find that the solid solution  $\text{Mg}_{1-x}\text{Cu}_x\text{Cr}_2\text{O}_4$  has a two-phase coexistence of cubic and tetragonal phases at room temperature for  $0.43 \leq x \leq 0.47$ . Tetragonality is induced by increasing JT activity in tetrahedrally coordinated  $\text{Cu}^{2+}$ . The average structure descriptions from Rietveld refinement provide an adequate description of the structures across the range of  $x$  and temperature. This is corroborated by the magnetic behavior, which indicates



a disordered atomic mixture. The  $x = 0.20$  sample is cooperatively JT distorted with orbital ordering at 15 K despite 82% of all  $\text{Cu}^{2+}$  having zero or only one  $\text{Cu}^{2+}$  neighbors.

Least-squares PDF refinements achieve good fits using the models from Rietveld refinement, implying that it might be difficult to improve on models where  $\text{CuO}_4$  and  $\text{MgO}_4$  are equivalent. Still, bond valence calculations show that RMC simulations produce better fits to the data while retaining chemically reasonable bond distances. The  $\text{AO}_4$  tetrahedral distortion increases with  $x$  as judged by CSM. The absence of distinct  $\text{CuO}_4$  local distortions in the low- $x$  CSM histograms does not prohibit their existence. When  $x = 0.43$ , tetrahedral DM indicate distinct coordination of  $\text{Cu}^{2+}$  versus  $\text{Mg}^{2+}$ . Furthermore, cation-cation interactions probed by  $\text{AA}_4$  CSM indicate that local clustering of Cu leads to increased JT distortion. This technique resolves cation-dependent JT distortions (even when they are incoherent) in materials where contrast between cations exists. The presence of magnetic exchange bias implies that short-range structural details are influencing the magnetic interactions, and more complex magnetic characterization may help describe these interactions.

## ACKNOWLEDGMENTS

We thank Maosheng Miao, Katharine Page, Graham King, Anna Llobet, and Thomas Proffen for helpful discussions. Details of  $\text{AA}_4$  correlations were investigated at the suggestion of a referee. This work has benefited from the use of NPfD at the Lujan Center at Los Alamos Neutron Science Center, funded by DOE Office of Basic Energy Sciences. Los Alamos National Laboratory is operated by Los Alamos National Security LLC under DOE Contract DE-AC52-06NA25396. This work was supported by the Institute for Multiscale Materials Studies and the National Science Foundation (DMR 0449354). The MRL Central Facilities are supported by the MRSEC Program of the NSF (DMR 05-20415); a member of the NSF-funded Materials Research Facilities Network ([www.mrfln.org](http://www.mrfln.org)).

---

\* Electronic address: [dshoe@mrl.ucsb.edu](mailto:dshoe@mrl.ucsb.edu)

† Electronic address: [seshadri@mrl.ucsb.edu](mailto:seshadri@mrl.ucsb.edu)

- [1] J. G. Bednorz and K. A. Müller, Z. Phys. B. **64**, 189 (1986).
- [2] E. Pavarini, I. Dasgupta, T. Saha-Dasgupta, O. Jepsen, and O. K. Andersen, Phys. Rev. Lett. **87**, 047003 (2001).
- [3] H. A. Jahn and E. Teller, Proc. R. Soc. A **161**, 220 (1937).
- [4] M. Gerloch, Inorg. Chem. **20**, 638 (1981).
- [5] X. Qiu, T. Proffen, J. Mitchell, and S. Billinge, Phys. Rev. Lett. **94** (2005).
- [6] A. Sartbaeva, S. A. Wells, M. F. Thorpe, E. S. Bozin, and S. J. L. Billinge, Phys. Rev. Lett. **99**, 155503 (2007).
- [7] E. Dagotto, *Nanoscale phase separation and colossal magnetoresistance: the physics of manganites and related compounds* (Springer, 2003).
- [8] J. B. Goodenough and A. L. Loeb, Phys. Rev. **116**, 32 (1955).
- [9] R. Engelman and B. Halperin, Phys. Rev. B **2**, 75 (1970).
- [10] M. Uehara, S. Mori, C. H. Chen, and S. Cheong, Nature **399**, 560 (1999).
- [11] S. Yeo, Y. Horibe, S. Mori, C. M. Tseng, C. H. Chen, A. G. Khachatryan, C. L. Zhang, and S. Cheong, Appl. Phys. Lett. **89**, 233120 (2006).
- [12] C. L. Zhang, S. Yeo, Y. Horibe, Y. J. Choi, S. Guha, M. Croft, S. Cheong, and S. Mori, Appl. Phys. Lett. **90**, 133123 (2007).
- [13] S. Park, Y. Horibe, T. Asada, L. S. Wielunski, N. Lee, P. L. Bonanno, S. M. O'Malley, A. A. Sirenko, A. Kazimirov, M. Tanimura, et al., Nano Lett. **8**, 720 (2008).
- [14] C. Leroux, A. Loiseau, D. Broddin, and G. Vantendelo, Phil. Mag. B **64**, 57 (1991).
- [15] Y. Le Bouar, A. Loiseau, and A. G. Khachatryan, Acta Mater. **46**, 2777 (1998).
- [16] P. Fratzl, O. Penrose, and J. L. Lebowitz, J. Stat. Phys. **95**, 1429 (1999).
- [17] J. L. MacManus-Driscoll, Adv. Func. Mater. **20**, 2035 (2010).
- [18] L.-Q. Yan, F. Maciá, Z.-W. Jiang, J. Shen, L.-H. He, and F.-W. Wang, J. Phys. Cond. Mat. **20**, 255203 (2008).
- [19] Y. Kino and S. Miyahara, J. Phys. Soc. Japan **21**, 2732 (1966).
- [20] L. Q. Yan, Z. W. Jiang, X. D. Peng, L. H. He, and F. W. Wang, Powder Diffraction **22**, 340 (2007).
- [21] S. Waplak and W. Bednarski, J. Phys. Cond. Mat. **14**, 12529 (2002).
- [22] H. Noh, S. Yeo, J. Kang, C. L. Zhang, S. Cheong, S. Oh, and P. D. Johnson, Appl. Phys. Lett. **88**, 081911 (2006).
- [23] D. P. Shoemaker, J. Li, and R. Seshadri, J. Am. Chem. Soc. **131**, 11450 (2009).
- [24] R. L. McGreevy, Nucl. Instrum. Meth. A **354**, 1 (1995).
- [25] R. L. McGreevy, J. Phys. Cond. Mat. **13**, R877 (2001).
- [26] S. T. Norberg, I. Ahmed, S. Hull, D. Marrocchelli, and P. A. Madden, J. Phys. Cond. Mat. **21**, 5401 (2009).
- [27] O. Cambon, J. Haines, M. Cambon, D. A. Keen, M. G. Tucker, L. Chapon, N. K. Hansen, M. Souhassou, and F. Porcher, Chem. Mater. **21**, 237 (2009).
- [28] A. L. Goodwin, S. Redfern, M. T. Dove, D. A. Keen, and M. G. Tucker, Phys. Rev. B **76**, 174114 (2007).
- [29] S. Wells, M. T. Dove, and M. G. Tucker, J. Appl. Cryst. **37**, 536 (2004).
- [30] H. Zabrodsky, S. Peleg, and D. Avnir, J. Am. Chem. Soc. **114**, 7843 (1992).
- [31] M. Pinsky and D. Avnir, Inorg. Chem. **37**, 5575 (1998).
- [32] S. Keinan and D. Avnir, J. Chem. Soc., Dalton Trans. pp. 941–947 (2001).
- [33] K. M. Ok, P. S. Halasyamani, D. Casanova, M. Llunell, P. Alemany, and S. Alvarez, Chem. Mater. **18**, 3176 (2006).
- [34] D. P. Shoemaker, R. Seshadri, A. L. Hector, A. Llobet, T. Proffen, and C. J. Fennie, Phys. Rev. B **81**, 144113 (2010).
- [35] J.-F. Bérar and G. Baldinozzi, IUCr-CPD Newsletter **20**,

- 3 (1998).
- [36] A. Larson and R. Von Dreele, Los Alamos National Laboratory Report LAUR **86**, 748 (2000).
  - [37] P. F. Peterson, M. Gutmann, T. Proffen, and S. J. L. Billinge, *J. Appl. Cryst.* **33**, 1192 (2000).
  - [38] C. L. Farrow, P. Juhas, J. W. Liu, D. Bryndin, E. S. Bozin, J. Bloch, T. Proffen, and S. J. L. Billinge, *J. Phys. Cond. Mat.* **19**, 335219 (2007).
  - [39] J. Li, *Modelling and Simul. Mater. Sci. Eng.* **11**, 173 (2003).
  - [40] K. Momma and F. Izumi, *J. Appl. Cryst.* **41**, 653 (2008).
  - [41] M. G. Tucker, D. A. Keen, M. T. Dove, A. L. Goodwin, and Q. Hui, *J. Phys. Cond. Mat.* **19**, 335218 (2007).
  - [42] N. E. Brese and M. O’Keeffe, *Acta Cryst. B* **47**, 192 (1991).
  - [43] A. Miller, *J. Appl. Phys.* **30**, S24 (1959).
  - [44] R. D. Shannon, *Acta Cryst. A* **32**, 751 (1976).
  - [45] W. A. Dollase and H. S. C. O’Neill, *Acta Cryst. C* **53**, 657 (1997).
  - [46] N. N. Greenwood and A. Earnshaw, *Chemistry of the Elements, II Edn.* (Butterworth-Heinemann, London, 1997).
  - [47] M. C. Day and J. Selbin, *Theoretical inorganic chemistry* (Rheinhold, New York, 1962).
  - [48] E. J. W. Verwey and E. L. Heilmann, *J. Chem. Phys.* **15**, 174 (1947).
  - [49] B. J. Kennedy and Q. Zhou, *J. Solid State Chem.* **181**, 2227 (2008), ISSN 0022-4596.
  - [50] M. Tovar, R. Torabi, C. Welker, and F. Fleischer, *Physica B* **385-386**, 196 (2006).
  - [51] H. Ehrenberg, M. Knapp, C. Baehtz, and S. Klemme, *Powder Diffr.* **17**, 230 (2002).
  - [52] S. Klemme and M. Ahrens, *Phys. Chem. Minerals* **34**, 59 (2007).
  - [53] L. Ortega-San-Martín, A. J. Williams, C. D. Gordon, S. Klemme, and J. P. Attfield, *J. Phys. Cond. Mat.* **20**, 104238 (2008).
  - [54] Z. Zhang, D. Louca, A. Visinuiu, S. Lee, J. Thompson, T. Proffen, A. Llobet, Y. Qiu, S. Park, and Y. Ueda, *Phys. Rev. B* **74** (2006).
  - [55] D. P. Shoemaker, E. E. Rodriguez, R. Seshadri, I. S. Abumohor, and T. Proffen, *Phys. Rev. B* **80**, 144422 (2009).
  - [56] S. C. van der Marck, *Phys. Rev. E* **55**, 1514 (1997).
  - [57] D. Reinen, M. Atanasov, G. Nikolov, and F. Steffens, *Inorg. Chem.* **27**, 1678 (1988).
  - [58] Y. Kino, B. Lüthi, and M. E. Mullen, *J. Phys. Soc. Japan* **33**, 687 (1972).
  - [59] M. O’Keeffe, *J. Phys. Chem. Solids* **21**, 172 (1961).
  - [60] P. Holba, M. Nevriya, and E. Pollert, *Mater. Res. Bull.* **10**, 853 (1975).
  - [61] D. G. Wickham and W. J. Croft, *J. Phys. Chem. Solids* **7**, 351 (1958).
  - [62] G. T. Bhandage and H. V. Keer, *J. Phys. C Solid State Phys.* **11**, L219 (1978).
  - [63] E. S. Bozin, M. Schmidt, A. J. DeConinck, G. Paglia, J. F. Mitchell, T. Chatterji, P. G. Radaelli, T. Proffen, and S. J. L. Billinge, *Phys. Rev. Lett.* **98**, 137203 (2007).
  - [64] D. Louca and J. Sarrao, *Phys. Rev. Lett.* **91** (2003).
  - [65] V. F. Sears, *Neutron News* **3**, 26 (1992).
  - [66] M. G. Tucker, M. P. Squires, M. T. Dove, and D. A. Keen, *J. Phys. Cond. Mat.* **13**, 403 (2001).
  - [67] H. Walter, I. Schulz, and J. Scheve, *Z. Anorg. Allg. Chem.* **352**, 241 (1967).
  - [68] H. Shaked, J. M. Hastings, and L. M. Corliss, *Phys. Rev. B* **1**, 3116 (1970).
  - [69] W. H. Meiklejohn and C. P. Bean, *Phys. Rev.* **102**, 1413 (1956).
  - [70] A. E. Berkowitz and K. Takano, *J. Magn. Magn. Mat.* **200**, 552 (1999).
  - [71] J. Nogués, J. Sort, V. Langlais, V. Skumryev, S. Suriñach, J. S. Muñoz, and M. D. Baró, *Physics Reports* **422**, 65 (2005).
  - [72] S. A. Makhlof, F. T. Parker, and A. E. Berkowitz, *Phys. Rev. B* **55**, R14717 (1997).
  - [73] B. Martínez, X. Obradors, L. Balcells, A. Rouanet, and C. Monty, *Phys. Rev. Lett.* **80**, 181 (1998).
  - [74] M. Ali, P. Adie, C. H. Marrows, D. Greig, B. J. Hickey, and R. L. Stamps, *Nat. Mater.* **6**, 70 (2007).
  - [75] V. A. M. Brabers, *J. Phys. Chem. Solids* **32**, 2181 (1971).